

Beamline setup for in situ measurements of particles in turbulent spray flames using small angle X-ray scattering

Mira Simmler^{a, *}, Manuel Meier^a, Luisa Rank^{a, b}, Gernot Buth^b,
Anton Plech^b, Hermann Nirschl^a

^a*Institute of Mechanical Process Engineering and Mechanics, Karlsruhe Institute of Technology, 76131 Karlsruhe, Germany*

^b*Institute for Photon Science and Synchrotron Radiation, Karlsruhe Institute of Technology, 76344 Eggenstein-Leopoldshafen, Germany*

Abstract

The particle formation in spray flame synthesis (SFS) is a fast and complex process involving many sub-steps that may happen simultaneously. To investigate the mechanisms that typically lead to small aggregated primary particles, a sophisticated technique for in situ measurements in the flame is necessary to provide information about primary particles and the aggregates as well. This work describes the development of an in situ measurement setup using small angle X-ray scattering (SAXS) to investigate the entire particle formation mechanism of zirconia nanoparticles in and above a turbulent spray flame. In preparation for the in situ measurements, a beamline for single crystal diffractometry at Karlsruhe Research Accelerator (KARA) was adapted for low scattering SAXS experiments including optimizations of the optics and measurement protocol. As a result, a significant dependence of scattering intensity was detected as a function of the height above the burner. A detailed analysis of the SAXS data and comparison with TEM images allow insights into the primary particle growth, the development of fractal properties and the aggregation process.

Keywords: Small angle X-ray scattering; Spray flame synthesis; In situ; Particle formation; Fractal structures

1. Introduction

Gas phase processes are nowadays commonly used to produce functionalized nanoparticles of different compounds [1–5]. Spray flame synthesis (SFS), in particular, offers significant advantages in terms of cost efficient precursor material and po-

tential for an easy scale up at consistent high purity of the product [4].

A liquid precursor containing metal ions and a combustible organic solvent is atomized and fed into a self-sustaining gas flame. The spray ignites resulting in the formation of a spray flame. The decay of the precursor solution initiates the particle formation process and secondary particle structures develop along the process chain because of sintering and agglomeration [2,5]. Although the process of SFS is already used in industrial

* Corresponding author.

E-mail address: mira.simmler@kit.edu (M. Simmler).

productions, the particle formation process is not fully understood and therefore, the properties of the nanoparticles cannot easily be controlled without extensive empiric studies.

Typically, the structure-determining mechanisms in a flame can be described by three sub-processes: chemical reaction, coagulation and coalescence. While the chemical reaction of the precursor leads to nucleation (formation of primary particles) or particle surface growth, coagulation of the primary particles results in the formation of aggregates (secondary particles). Coalescence dominates the process in a high-temperature zone and leads to a reduced degree of aggregation, which can result in complete sintering to spherical particles [6–9]. Different models for a more detailed description of the particle formation mechanisms have already been developed for several particle systems. In the case of organometallic precursors, the aerosol droplets evaporate as soon as they enter the flame resulting in particle formation in the gas phase (gas-to-particle) [5,10]. The structure-determining sub-steps occur on different time scales. While the spray formation and evaporation are slow compared to the precursor decay, the flame chemistry happens considerably faster. The particle formation depends on the competition of coalescence and aggregation, which are both temperature-driven. Despite these insights, the knowledge and therefore, the control of this process is still limited. In situ measurements can help gain a more in-depth understanding.

Small angle X-ray scattering (SAXS) can provide numerous structural parameters like an averaged diameter of primary particles and aggregates or the fractal dimension of mass and surface over a wide range of sizes with just one acquisition. SFS products typically consist of small primary particles, which are sintered to each other to form larger aggregates with a wide size distribution. The analysis of the scattering data can be challenging because of the overlapping multiscale information. Several successful studies show the potential of SAXS for flame made products [11–13].

One of the few SAXS studies of particles produced by SFS is the work of Kammler et al. (2004). They investigated the production of silica particles in premixed and diffusion flame reactors and distinguished between gaseous and liquid injection of the precursor into the flame [14]. The produced particles were analyzed by means of transmission electron microscopy (TEM), nitrogen adsorption techniques and USAXS (ultra-small angle X-ray scattering) measurements. The USAXS results allowed for the distinction of agglomerated and non-agglomerated particle systems. Furthermore, these studies showed that in the case of the gaseous precursor feed the size of the aggregates or hard agglomerates was only slightly dependent on the flow rate. In the case of the SFS process, conversely, an increase of the flow rate led to an increase of

the aggregate size. In summary, a liquid precursor produces significantly smaller and more compact aggregates with larger primary particles than a gaseous one, likely due to higher temperatures and shorter residence times in the SFS process.

Starting in 1986, studies of soot generation demonstrated the benefit of SAXS analysis to obtain a deeper insight in nucleation processes and particle growth in the gas phase. Using high intensity synchrotron sources in particular allows for a non-invasive investigation of the particle formation in situ in the flame without sample retrieval [15–18]. These studies show the potential of SAXS measurements to describe complex aerosol dynamic processes and thus provide a profound comprehension of the overall process. In contrast to soot generation, there are only a few approaches to investigate flame synthesis for metal oxides using in situ SAXS.

In 2004, Beaucage was the first to probe the growth of oxide nanoparticles in a methane and oxygen diffusion flame in situ using the highly collimated monochromatic X-ray beam at the European Synchrotron Radiation Facility (ESRF) in Grenoble, France. A vaporous precursor of hexamethyl-disiloxane (HMDSO) produced colloidal silica particles growing from approximately 20 nm to 55 nm along the height of the flame [19].

Using the same setup, Kammler et al. carried out USAXS measurements at the Advanced Photon Source at Argonne National Laboratories in Chicago, USA to monitor the growth and aggregation of colloidal silica in a hot flame and silica aggregates in a cold flame [20]. The obtained data showed particles along the height above the burner, including primary particle diameter, mass fractal dimension and aggregate size that were in good agreement with intrusively obtained thermophoretically sampled TEM and static light scattering measurements.

In their in situ study of aggregate topology during growth of pyrolytic silica, Rai et al. (2018) showed the potential of in situ SAXS investigations of flame pyrolysis [21]. As a result, an extensive set of derived parameters including particle and aggregate properties allowed for a very broad analysis of the generated pyrogenic, strongly scattering silica structures.

Using a similar setup for the in situ investigation of silica, Camenzind et al. increased the oxygen flow turning the diffusion flame turbulent and observed the formation of fractal-like, aggregated nanoparticles [22].

In his review article of 2009, Narayanan showed the results of in situ measurements close to the nozzle of SFS for zirconia nanoparticles. SAXS data of the particles and spray droplets was collected up to 25 mm above the burner to investigate the nucleation and growth of the primary particles [23]. Additionally, results with the same setup are de-

scribed in the last chapter of the doctoral thesis by Jossen [24]. Here, the author successfully performed in situ investigations of the particle formation, growth and aggregation process in spray flames.

Previously, we outlined our approach to characterize fractal structures made by SFS using a SAXS laboratory camera in the data evaluation paper by Simmler et al. [25]. The transfer of these methods to low scattering in situ measurements in the flame is only possible with a synchrotron source since the flux of a laboratory X-ray source is not sufficient.

In this paper, we describe a SAXS setup at the beamline for single crystal diffractometry (SCD) at the Karlsruhe Research Accelerator (KARA) in Karlsruhe, Germany for in situ measurements of particle growth in SFS. The use of a standardized burner and the adaptation of this beamline for SAXS measurements makes this setup unique. The boundary conditions require a large cross section of open flame volume. Challenges with the background are tackled by hardware optimization and measuring routines. Results include measurements and analysis at different heights above the burner to describe the particle formation and aggregation process in and above the flame.

2. Experimental

2.1. Flame spray synthesis (SFS)

The burner in this setup is a standardized burner called *spraysyn* of the German priority program (SPP1980) of the German Research Foundation (DFG). This means a large group of scientists are characterizing the process of flame spray synthesis based on this burner using different measurement and simulation techniques. The burner consists of multiple annular orifices for the gas supply. To generate a spray flame, a liquid precursor is supplied by a syringe pump (Harvard Instruments, USA) at 2 ml min^{-1} through a cannula into the center of the burner and is atomized with 10 slm (standard liter per minute) oxygen through an annular gap around the cannula. Around this nozzle, a laminar self-sustaining pilot flame of 2 slm methane and 16 slm oxygen ignites the spray. The resulting turbulent spray flame is stabilized with 120 slm sheath air (pressured air). All gas flows are controlled by mass flow controllers (Bronkhorst, Germany). Fig. 1 shows a sectional view of the burner.

Additionally, Schneider et al. provide a detailed description and the design concept of the *spraysyn* burner as well as developed a routine to compare the resulting spray flames [26]. For the here presented setup, the quality of the pilot and spray flame in terms of flame symmetry, dimension and color was cross-checked accordingly. Computational fluid dynamics simulations of the spray flame show temperature profiles with highest tempera-

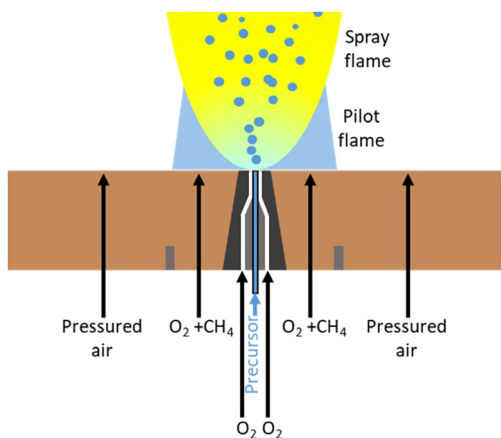


Fig. 1. Schematic illustration of the *spraysyn* burner.

tures of up to $2200 \text{ }^\circ\text{C}$ and a strong influence of the pilot flame [27,28].

The burner is mounted on a movable platform to position the flame in two directions relative to the beam of the synchrotron source. The burning chamber has a dimension of 500 mm in width, 500 mm in depth and 700 mm in height and is connected to an exhaust filter system. A gap in the walls at the bottom of the chamber allows the intake of false air preventing a build-up of a negative pressure in the chamber and subsequently a lift off of the pilot flame.

The precursor solutions consist of 0.5 mol l^{-1} zirconium(IV)-n-butoxide (80%(w/w) in butanol, Alfa Aesar) in 1-butanol (99.5% for analysis, Acros Organics).

Schneider et al. [26] and Martins et al. [27] investigated the spray properties for the *spraysyn* burner with the same operating parameters used here including the characterization of the gas velocity as well as the temperature profile along the height above the burner (HAB). As expected, the velocity is highest (approx. $60\text{--}80 \text{ m s}^{-1}$) in the center and between 10 and 20 mm above the nozzle, where the spray is fully developed. The further away from the nozzle in horizontal and vertical direction the lower is the velocity. However, in contrast to a diffusion flame, a complex flow field for the spray in the center and the surrounding flame was observed. Since the X-ray beam captures the whole transverse section of the flame, no clear residence time can be assigned to a certain HAB. Therefore, we present our data dependent on the HAB to enable a simple comparison with other characterization methods of the particles in the spray flame.

A hole-in-tube probe similar to Tischendorf et al. [29] was used to collect nanoparticles on a TEM-grid at different HABs above the flame and powder samples at $\text{HAB} = 120 \text{ mm}$ for SAXS measurements for a comparison with the in situ results.

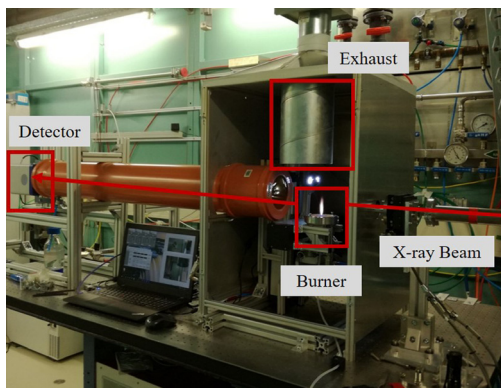


Fig. 2. Experimental setup for in situ SAXS measurements at the SCD beamline of KARA.

The TEM-grids were analyzed with JEOL JEM-2200FS at the Interdisciplinary Center for Analytics at the Nanoscale (ICAN) at the University Duisburg Essen, Germany.

2.2. Setup at synchrotron KARA

In situ measurements took place at the SCD beamline at KARA in Karlsruhe, Germany. The storage ring of the synchrotron was operated at 2.5 GeV and the wavelength was set to 0.1393 nm. Emitted by a dipole magnet, the beam is conditioned by primary slits and a sagittally bent double crystal monochromator for horizontal and a reflection mirror for vertical focusing. The focus was set to the detector position. An evacuated flight path guides the monochromatic beam to a 4-sector slit for size definition followed by an exchangeable pinhole of Germanium. The pinhole was laser-drilled from a single-crystalline wafer of 0.5 mm thickness.

As Fig. 2 shows, the burner was placed between the evacuated beam path on the source side and the following tube with the detector (Pilatus2 100K-S, Dectris Ltd., Switzerland) at the end for the scattered radiation.

To prevent the scattering from air molecules, the following tube was sealed with polyimide foils (Kapton, Dupont) and flooded with helium gas. A beam stop with a diameter of 4 mm shields the direct beam from entering the detector. An ionization chamber in the beam path is used to track X-ray flux before the 4-sector slit. As the burner is part of a standardized experiment with ample pre-characterization, we were required to operate the burner under specified conditions, which heated the burner and the surrounding environment. Since this experiment produces respirable nanoparticles, we had to comply with additional safety regulations to prevent any exposure. These circumstances combined lead to a beam path of 43 cm through air. The sample-to-detector distance was calibrated by using silver behenate and the program Fit2D. The

Table 1
Parameters of the detector calibration.

Sample to detector distance (mm)	1369.48
Wavelength (nm)	0.1393
Rotation angle of tilting plane (-)	178.73°
Angle of detector tilt in plane (-)	-2.06°

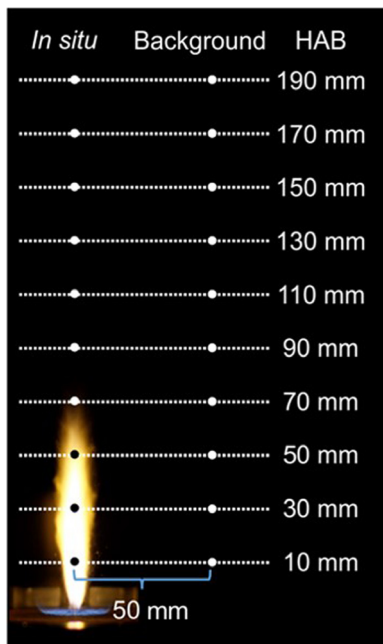


Fig. 3. Measurement points for in situ SAXS.

results of the calibration of the experimental setup are given in Table 1.

To detect even small differences in the scattering signal of the particles in the flame, a measurement routine that enables reproducible measurements independent of external influences such as setup drifts is necessary. During the data acquisition, the ionization chamber of the beamline records the direct beam intensity. This enables a correction of changes in the direct beam intensity. In addition, flame and background measurements were performed alternately similar to the routine of interleaving used by Reich et al. [30]. The data acquisition in the flame runs for 25 s at each position, which is indicated along the flame axis with HAB as shown in Fig. 3. Afterwards, the burner is moved out of the direct beam (50 mm) to conduct a background measurement of 25 s. For each measurement, this pair of measurements was repeated 20 times.

For all recorded detector images, the beam stop as well as dead pixels and the edge of the detector were combined in a mask excluding them from any further evaluation. To identify further conspicuous pixels, a standard deviation analysis

was performed. The values of all pixels of 25 nominally identical detector images (measuring time 5 s) were compared with each other and the standard deviations were plotted over the mean values. The pixel intensity was assumed to show a Poisson distribution, with the standard deviation scaling with the square root of intensity. The standard deviation σ of pixel rejection is set to values differing by more than $\pm 1\sigma$ leading to an exclusion of 1.65% of pixels. After the elimination of the bad pixels, an azimuthal integration of the pixel values around the beam center on the 2D detector image was performed to obtain the 1D scattering data with space-angle and polarization correction of the horizontally polarized beam. The data collected from the flame and the background was summed up separately to derive error margins. Then, the background-subtracted flame data was converted to absolute units using standardized glassy carbon.

2.3. Small angle X-ray scattering (SAXS)

The SAXS data is analyzed as $I(q)$ with q being the scattering vector:

$$q = 4\pi/\lambda \sin(\theta/2) \quad (1)$$

with λ being the wavelength of the X-ray beam and θ the scattering angle. The scattering intensity $I(q)$ of a polydisperse particle system with a distribution of the particle radius $f(r)$ can be expressed as

$$I(q) = N/V \Delta\rho_e^2 \int f(r) V_p(r)^2 P(q, r) dr \quad (2)$$

where N is number of particles in the sample volume V , $\Delta\rho_e$ the scattering contrast, $V_p(r)$ the volume of one particle and $P(q, r)$ the form factor defining the shape of the particles [31].

The *Unified Fit Model* (Irena Package 2.68 [32], IgorPro, WaveMetrics Inc.) according to Beaucage [33] is used to evaluate the collected scattering data by dividing it into different structural levels. Each level is assigned a power law fit and a Guinier fit. The power law fit provides information about morphology of the underlying structure, where the exponent p indicates the slope in a double logarithmic diagram. The Guinier fit, on the other hand, indicates the averaged characteristic size of the particles using the radius of gyration R_g . To compare this parameter with primary particle sizes of other measurement techniques, a mean diameter d_{R_g} can be calculated using R_g and the polydispersity index (PDI), which is based on the prefactors of both fits [13,16]. More details on the used methods can be found in the data evaluation paper [25].

The Kratky plot (I^*q^2 over q) connects every local scattering maximum to a structural level. The area under the curve, the so-called Porod invariant Q , provides information about the mass of the scattered particles [19].

$$Q = \int q^2 I(q) dq, \quad (3)$$

3. Results and discussion

As the setup needs to be suitable for low scattering experiments, the intensity of the incident beam is responsible for the signal to noise ratio of the results. In this setup, the last pinhole before the sample defines the shape and size of incident beam including the diffuse background.

In Fig. 4, the diffuse scattering through the 4-sector slit (gray squares) is shown compared to the added low-scatter pinhole (black dots) as well as a calibrant sample of monodisperse silica nanoparticles (Ludox HS-40) highly diluted in water (blue dots). It is evident that the 4-sector slit alone produces a strong and inhomogeneous background that is difficult to completely subtract from the data. The background with the Germanium pinhole is very homogenous and much lower. The corresponding SAXS signal from the silica particles after subtraction of water as background is reliable and can be modeled by sphere form factors up to higher maxima in oscillation. In a brief comparison, the same order of magnitude in scattering suppression is achieved with commercial no-scatter pinholes. All following results were obtained using the self-made pinhole.

The in situ measurements were performed between 10 mm and 190 mm HAB using a precursor concentration of 0.5 mol l^{-1} zirconium butoxide in butanol. Fig. 5 shows the scattering results in the flame from 10 to 70 mm HAB including error bars based on the standard error of the summed up SAXS data and the unified fit by Beaucage [33]. Considering the good signal-to-noise ratio, the setup is suitable for in situ SAXS measurements in a turbulent flame and in the same absolute intensity range as the results by Jossen [24]. The overall intensity increases and the signal-to-noise ratio for larger scattering vectors improves with growing

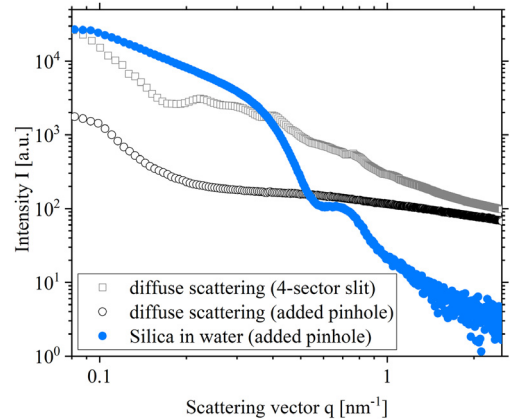


Fig. 4. Comparison of diffuse scattering of the background through the 4-sector slit and added pinhole and a calibrant.

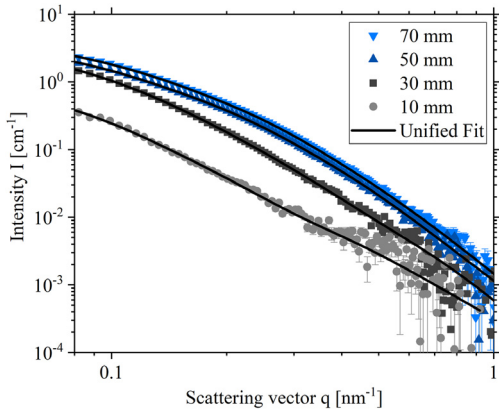


Fig. 5. In situ SAXS data for HAB 10–70 mm (in the flame).

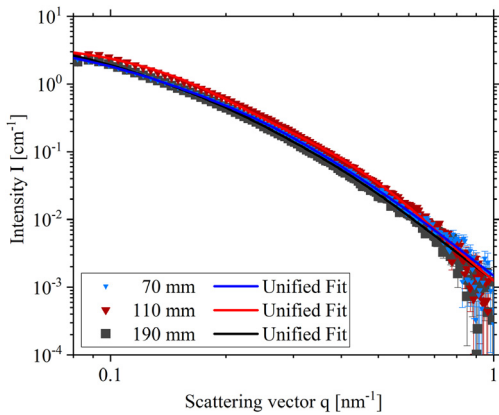


Fig. 6. In situ SAXS data for HAB 70–190 mm (above the flame).

HAB. This behavior confirms the existence of particles already at 10 mm HAB and shows a growth in size and number of the particles. Starting at HAB 50 mm, a Guinier region is clearly visible by the change of slope at $q = 0.2\text{--}0.4 \text{ nm}^{-1}$ allowing the determination of a radius of gyration and subsequently, a mean diameter for primary particles. The size of prospective large aggregates is beyond the q resolution of the setup.

Moving above the flame (Fig. 6), the intensity and shape of the scattering does not change noticeably from 70 to 190 mm HAB. As the shape of the scattering curve stays the same, the particle formation and aggregation process seems to end at the tip of the flame at 70 mm HAB.

To compare these results, TEM samples were extracted above the flame using a hole-in-tube probe. Fig. 7 shows TEM images of the same HABs as Fig. 6 in two magnifications. The images with lower magnification reveal aggregates of different sizes for 70–190 mm HAB. With distance from the burner, fewer single particles appear and the

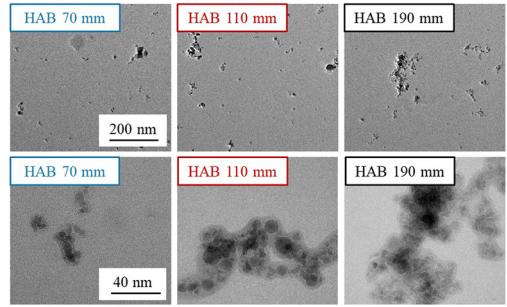


Fig. 7. TEM images in two magnifications of zirconia nanoparticles extracted for HAB 70–190 mm (above the flame).

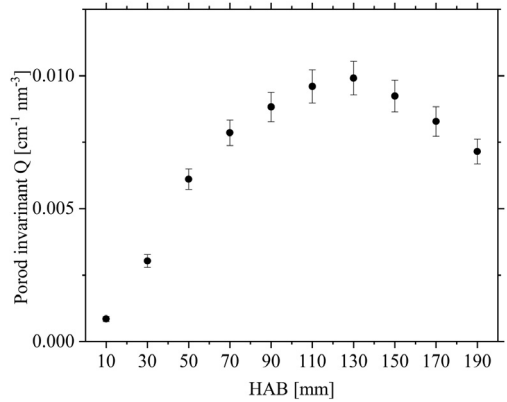


Fig. 8. Porod invariant of in situ SAXS data at different HABs.

aggregate size, although very polydisperse, seems to increase. In contrast to the SAXS results, this suggests an ongoing aggregation above the flame. However, this is only one image of a few particles whereas the SAXS measurements sample a temporal and spatial cross section of the beam through the width of the flame.

The images with higher magnification show the primary particles. The average size and polydispersity of the particles appear to stay constant confirming a full formation of the primary particles above the flame.

To obtain a better visualization of the results, the Porod invariant was calculated for each scattering data set using Eq. (3) (see Fig. 8). The highest value for Q is reached at 130 mm HAB showing the highest scattering volume. Here, the particle formation is finished and the particle number density is highest. In the flame up to 70 mm HAB, the increase in Q appears linear showing the combined effect of particle formation, growth and aggregation on the scattering volume. Above the flame up to 130 mm HAB, Q is still growing albeit slower suggesting ongoing particle growth and aggregation. The decrease of Q above 130 mm HAB, is a result

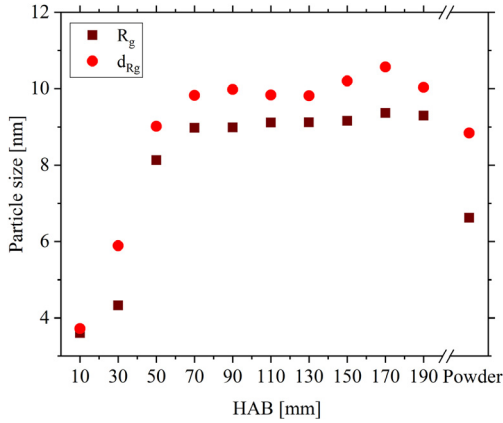


Fig. 9. Radius of Gyration and diameter based on radius of Gyration from SAXS scattering data at different HABs and from the powder sample.

of the dilution of the particles by air high above the flame. These results confirm our findings so far and show signs of aggregation above the flame not visible in the scattering data in Fig. 6 but in the TEM images of Fig. 7.

Since an increase in Q can have multiple causes, the next step is the determination of the primary particle size in and above the flame. Fig. 9 shows the radius of Gyration R_g determined by the Guinier fit (see Fig. 6) and the calculated diameter d_{Rg} based on this fit and the PDI. While R_g is always lower than d_{Rg} , both show the same trend. Contrary to expectations, d_{Rg} is not twice R_g . In case of polydisperse particles, SAXS measurements overestimate larger particles in comparison to small ones. The PDI in the calculation of the mean diameter d_{Rg} corrects this fact leading to a lower result [19].

For the in situ measurements, this means a particle growth from almost 4 nm to 9–10 nm from 10 to 70 mm HAB and staying this size till 190 mm HAB. These results are in good agreement with Jossen's in his last chapter [24]. The values of the powder sample (last datapoint in the diagram) are slightly lower than the in situ results. However, the powder was collected in a different experiment at a different day. The polydispersity of the primary particles is very high as is apparent in the TEM images (Fig. 7) and the slow change of slope in Guinier region $q = 0.2\text{--}0.4 \text{ nm}^{-1}$ (see Fig. 6). This leads to slight changes in the mean particle size between experiments.

Nonetheless, these results confirm on the one hand the growth of primary particles in the flame and on the other hand the termination of the formation at the tip of the flame.

The last step is the analysis of the fractal properties to investigate the aggregation of the particles. In Fig. 10, the slope p of both power law fits for the first and second structural level is plotted over

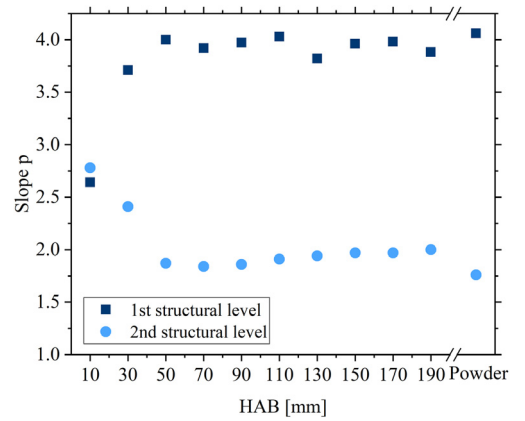


Fig. 10. Slope p of the Power Law Fit from SAXS scattering data for both structural levels at different HABs and from the powder sample.

the HAB. The first structural level describes the primary particles with their size using the Guinier fit (Fig. 9) and their fractal dimension of surface using the power law fit at larger scattering vectors $q < 0.5 \text{ nm}^{-1}$. The slope p can obtain values between 3 and 4 describing very rough to smooth surfaces of the primary particles [34]. The in situ measurements show rough surfaces in the flame turning smooth starting at 50 mm HAB. This phenomenon can be connected to the primary particle growth in the flame (Fig. 9) since the particles did not have time to perfect their spherical shape. The fact that smaller particles also have a greater surface to volume ratio could explain why these imperfections on the surface have a stronger impact on smaller particles.

In the second structural level at small scattering vectors $q < 0.2 \text{ nm}^{-1}$, the shape of the aggregates can be characterized with the fractal dimension of mass using the slope p as well. Here, the value of p refers directly to the dimension of the aggregate [34]. The slope p decreases from 2.8 to 1.7 in the flame illustrating the development from three dimensional to flaky aggregates. Although the slope p does not indicate the size, this decline suggests aggregation as small aggregates can only assume a spherical form and can only develop a specific shape through growth. The value of 1.7 is very typical for flame made products [12]. Above the flame, no significant change of the slope p takes place suggesting that the aggregates still increase in size but do not change their general shape.

4. Conclusion

In this work we presented a beamline setup and measurement protocol to perform in situ SAXS measurements in a turbulent spray flame to gain information about the particle formation process. In

situ measurements show that this setup at a SCD beamline with optimizations regarding the optics and measurement routine is suitable for low scattering experiments in a turbulent spray flame.

The collected SAXS data at different height above the burner were analyzed using the unified fit by Beaucage and the Porod invariant. Combined, these tools show a growth of primary particles and simultaneously the aggregation of them in the flame. The particle growth also leads to smooth surfaces of the primary particles. Above the flame, neither the size of the primary particles nor the fractal dimension of mass changes anymore. However, TEM images and the Porod invariant suggest further aggregation above the flame. These results fit the particle formation model “gas-to-particle” and confirm that SAXS can be used for in situ measurements in turbulent flames to detect the formation and growth of nanoparticles in spray flame synthesis.

Declaration of Competing Interest

The authors declare that they have no known competing financial interests or personal relationships that could have appeared to influence the work reported in this paper.

Acknowledgments

The research leading to these results has received funding from the German Research Foundation (DFG) within the priority program SPP 1980 spraysyn (Ni 414/30-1 and Ni 414/30-2).

We acknowledge provision of beam time and would like to thank the Institute for Beam Physics and Technology (IBPT) for the operation of the storage ring, the Karlsruhe Research Accelerator (KARA).

References

- [1] C. Schulz, T. Dreier, M. Fikri, H. Wiggers, Gas-phase synthesis of functional nanomaterials: Challenges to kinetics, diagnostics, and process development, *Proc. Combust. Inst.* 37 (1) (2019) 83–108, doi:[10.1016/j.proci.2018.06.231](https://doi.org/10.1016/j.proci.2018.06.231).
- [2] W.Y. Teoh, R. Amal, L. Mädler, Flame spray pyrolysis: An enabling technology for nanoparticles design and fabrication, *Nanoscale* 2 (8) (2010) 1324–1347, doi:[10.1039/C0NR00017E](https://doi.org/10.1039/C0NR00017E).
- [3] S.E. Pratsinis, Flame aerosol synthesis of ceramic powders, *Prog. Energy Combust. Sci.* 24 (3) (1998) 197–219, doi:[10.1016/S0360-1285\(97\)00028-2](https://doi.org/10.1016/S0360-1285(97)00028-2).
- [4] F. Meierhofer, U. Fritsching, Synthesis of Metal Oxide Nanoparticles in Flame Sprays: Review on Process Technology, Modeling, and Diagnostic, *Energy Fuels* 35 (7) (2021) 5495–5537, doi:[10.1021/acs.energyfuels.0c04054](https://doi.org/10.1021/acs.energyfuels.0c04054).

- [5] A. Purwanto, W.-N. Wang, K. Okuyama, in: N. Ashgriz (Ed.), *Handbook of Atomization and Sprays: Theory and Applications*, vol. 17, Springer Science+Business Media LLC, Boston, MA, 2011, pp. 869–879.
- [6] M.L. Eggersdorfer, S.E. Pratsinis, The Structure of Agglomerates consisting of Polydisperse Particles, *Aerosol Sci. Technol.* 46 (3) (2012) 347–353, doi:[10.1080/02786826.2011.631956](https://doi.org/10.1080/02786826.2011.631956).
- [7] M.L. Eggersdorfer, S.E. Pratsinis, Restructuring of aggregates and their primary particle size distribution during sintering, *AIChE J.* 59 (4) (2013) 1118–1126, doi:[10.1002/aic.14043](https://doi.org/10.1002/aic.14043).
- [8] M.L. Eggersdorfer, S.E. Pratsinis, Agglomerates and aggregates of nanoparticles made in the gas phase, *Adv. Powder Technol.* 25 (1) (2014) 71–90, doi:[10.1016/j.apt.2013.10.010](https://doi.org/10.1016/j.apt.2013.10.010).
- [9] A. Gutsch, J. Averdung, H. Mühlenweg, Von der technischen Entwicklung zum erfolgreichen nanotechnologischen Produkt, *Chem. Ingenieur Tech.* 77 (9) (2005) 1377–1392, doi:[10.1002/cite.200500116](https://doi.org/10.1002/cite.200500116).
- [10] R. Strobel, S.E. Pratsinis, Flame aerosol synthesis of smart nanostructured materials, *J. Mater. Chem.* 17 (45) (2007) 4743, doi:[10.1039/b711652g](https://doi.org/10.1039/b711652g).
- [11] D.W. Schaefer, A.J. Hurd, Growth and Structure of Combustion Aerosols: Fumed Silica, *Aerosol Sci. Technol.* 12 (4) (1990) 876–890, doi:[10.1080/02786829008959400](https://doi.org/10.1080/02786829008959400).
- [12] C.M. Sorensen, Light Scattering by Fractal Aggregates: A Review, *Aerosol Sci. Technol.* 35 (2) (2001) 648–687, doi:[10.1080/02786820117868](https://doi.org/10.1080/02786820117868).
- [13] G. Beaucage, H.K. Kammler, S.E. Pratsinis, Particle size distributions from small-angle scattering using global scattering functions, *J. Appl. Crystallogr.* 37 (4) (2004) 523–535, doi:[10.1107/S0021889804008969](https://doi.org/10.1107/S0021889804008969).
- [14] H.K. Kammler, G. Beaucage, R. Mueller, S.E. Pratsinis, Structure of Flame-Made Silica Nanoparticles by Ultra-Small-Angle X-ray Scattering, *Langmuir* 20 (5) (2004) 1915–1921, doi:[10.1021/la030155v](https://doi.org/10.1021/la030155v).
- [15] C. Gardner, G.N. Greaves, G.K. Hargrave, S. Jarvis, P. Wildman, F. Meneau, W. Bras, G. Thomas, In situ measurements of soot formation in simple flames using small angle X-ray scattering, *Nucl. Instrum. Methods Phys. Res. Sect. B: Beam Interact. Mater. Atoms* 238 (1–4) (2005) 334–339, doi:[10.1016/j.nimb.2005.06.072](https://doi.org/10.1016/j.nimb.2005.06.072).
- [16] M. Sztucki, T. Narayanan, G. Beaucage, In situ study of aggregation of soot particles in an acetylene flame by small-angle x-ray scattering, *J. Appl. Phys.* 101 (11) (2007) 114304, doi:[10.1063/1.2740341](https://doi.org/10.1063/1.2740341).
- [17] W.A. ENGLAND, An In Situ X-Ray Small Angle Scattering Study of Soot Morphology in Flames, *Combust. Sci. Technol.* 46 (1–2) (1986) 83–93, doi:[10.1080/00102208608959793](https://doi.org/10.1080/00102208608959793).
- [18] J.P. Hessler, S. Seifert, R.E. Winans, T.H. Fletcher, Small-angle X-ray studies of soot inception and growth, *Faraday Disc* 119 (1) (2001) 395–407, doi:[10.1039/B102822G](https://doi.org/10.1039/B102822G).
- [19] G. Beaucage, H.K. Kammler, R. Mueller, R. Strobel, N. Agashe, S.E. Pratsinis, T. Narayanan, Probing the dynamics of nanoparticle growth in a flame using synchrotron radiation, *Nat. Mater.* 3 (6) (2004) 370–374, doi:[10.1038/nmat1135](https://doi.org/10.1038/nmat1135).

- [20] H.K. Kammler, G. Beaucage, D.J. Kohls, N. Agashe, J. Ilavsky, Monitoring simultaneously the growth of nanoparticles and aggregates by in situ ultra-small-angle x-ray scattering, *J. Appl. Phys.* 97 (5) (2005) 54309, doi:[10.1063/1.1855391](https://doi.org/10.1063/1.1855391).
- [21] D.K. Rai, G. Beaucage, K. Vogtt, J. Ilavsky, H.K. Kammler, In situ study of aggregate topology during growth of pyrolytic silica, *J. Aerosol Sci.* 118 (2018) 34–44, doi:[10.1016/j.jaerosci.2018.01.006](https://doi.org/10.1016/j.jaerosci.2018.01.006).
- [22] A. Camenzind, H. Schulz, A. Teleki, G. Beaucage, T. Narayanan, S.E. Pratsinis, Nanostructure Evolution: From Aggregated to Spherical SiO₂ Particles Made in Diffusion Flames, *Eur. J. Inorg. Chem.* 2008 (6) (2008) 911–918, doi:[10.1002/ejic.200701080](https://doi.org/10.1002/ejic.200701080).
- [23] T. Narayanan, High brilliance small-angle X-ray scattering applied to soft matter, *Curr. Opin. Colloid Interface Sci.* 14 (6) (2009) 409–415, doi:[10.1016/j.cocis.2009.05.005](https://doi.org/10.1016/j.cocis.2009.05.005).
- [24] R. Jossen, *Controlled Synthesis of Mixed Oxide Nanoparticles by Flame Spray Pyrolysis*, ETH Zurich, Switzerland, 2006.
- [25] M. Simmler, M. Meier, H. Nirschl, Characterization of Fractal Structures by Spray Flame Synthesis Using X-ray Scattering, *Materials* (Basel, Switzerland) 15 (6) (2022), doi:[10.3390/ma15062124](https://doi.org/10.3390/ma15062124).
- [26] F. Schneider, *Optical in Situ Characterization of Lab-Scale and Pilot-Scale Burners for Nanoparticle Synthesis*, University of Duisburg-Essen, Germany, 2020.
- [27] F.J. Martins, J. Kirchmann, A. Kronenburg, F. Beyrau, Experimental investigation of axisymmetric, turbulent, annular jets discharged through the nozzle of the SPP1980 SpraySyn burner under isothermal and reacting conditions, *Exp. Thermal Fluid Sci.* 114 (2020) 110052, doi:[10.1016/j.expthermflusci.2020.110052](https://doi.org/10.1016/j.expthermflusci.2020.110052).
- [28] F. Schneider, S. Suleiman, J. Menser, E. Borukhovich, I. Wlokas, A. Kempf, H. Wiggers, C. Schulz, SpraySyn - A standardized burner configuration for nanoparticle synthesis in spray flames, *Rev. Sci. Instrum.* 90 (8) (2019) 85108, doi:[10.1063/1.5090232](https://doi.org/10.1063/1.5090232).
- [29] R. Tischendorf, M. Simmler, C. Weinberger, M. Bieber, M. Reddemann, F. Fröde, J. Lindner, H. Pitsch, R. Kneer, M. Tiemann, H. Nirschl, H.-J. Schmid, Examination of the evolution of iron oxide nanoparticles in flame spray pyrolysis by tailored in situ particle sampling techniques, *J. Aerosol Sci.* 154 (2021) 105722, doi:[10.1016/j.jaerosci.2020.105722](https://doi.org/10.1016/j.jaerosci.2020.105722).
- [30] S. Reich, A. Letzel, A. Menzel, N. Kretzschmar, B. Gökce, S. Barcikowski, A. Plech, Early appearance of crystalline nanoparticles in pulsed laser ablation in liquids dynamics, *Nanoscale* 11 (14) (2019) 6962–6969, doi:[10.1039/C9NR01203F](https://doi.org/10.1039/C9NR01203F).
- [31] H. Nirschl, X. Guo, Characterisation of structured and functionalised particles by small-angle X-ray scattering (SAXS), *Chem. Eng. Res. Design* 136 (2018) 431–446, doi:[10.1016/j.cherd.2018.06.012](https://doi.org/10.1016/j.cherd.2018.06.012).
- [32] J. Ilavsky, P.R. Jemian, Irena tool suite for modeling and analysis of small-angle scattering, *J. Appl. Crystallogr.* 42 (2) (2009) 347–353, doi:[10.1107/S0021889809002222](https://doi.org/10.1107/S0021889809002222).
- [33] G. Beaucage, Small-Angle Scattering from Polymeric Mass Fractals of Arbitrary Mass-Fractal Dimension, *J. Appl. Crystallogr.* 29 (2) (1996) 134–146, doi:[10.1107/S0021889895011605](https://doi.org/10.1107/S0021889895011605).
- [34] Y. No, R.-J. Roe, *Methods of X-ray and Neutron Scattering in Polymer Science*, Oxford Univ. Press, New York, NY, 2000.